PHYSICAL REVIEW C **82**, 035802 (2010)

^{16}O(α,γ)^{20}Ne *S* factor: Measurements and *R*-matrix analysis

H. Costantini,[1,2] R. J. deBoer,[2,*] R. E. Azuma,[2,3] M. Couder,[2] J. Görres,[2] J. W. Hammer,[2,†] P. J. LeBlanc,[2] H. Y. Lee,[4]
S. O'Brien,[2] A. Palumbo,[2] E. C. Simpson,[5] E. Stech,[2] W. Tan,[2] E. Uberseder,[2] and M. Wiescher[2]
[1]*Instituto Nazionale di Fisica Nucleare, Sezione di Genova, Genova, Italy*
[2]*Department of Physics, University of Notre Dame, Notre Dame, Indiana 46556, USA*
[3]*Department of Physics, University of Toronto, Toronto, Ontario M5S 1A7, Canada*
[4]*LANLSCE-NE, Los Alamos National Laboratory, New Mexico 87545, USA*
[5]*Department of Physics, Faculty of Engineering and Physical Sciences, University of Surrey, Guildford, Surrey GU2 7XH, United Kingdom*
(Received 28 June 2010; published 13 September 2010)

The article presents new measurements of low-energy resonances in the ^{16}O(α,γ)^{20}Ne reaction, which represents the endpoint for the reaction sequence responsible for energy production in stellar helium burning in massive red giant stars. The present data and previous unpublished data are analyzed in the framework of *R*-matrix theory to derive a reaction rate for the temperature regime of stellar helium burning.

DOI: 10.1103/PhysRevC.82.035802 PACS number(s): 26.20.Fj, 21.10.Jx, 25.55.Hp, 27.20.+n

I. INTRODUCTION

The ^{16}O(α,γ)^{20}Ne reaction ($Q = 4.730$ MeV) is important in stellar He-burning. At quiescent He-burning temperatures, the reaction rate is considered to be low due to the lack of resonances in the relevant energy region ($E_{\text{c.m.}}$ ~300 keV). This reaction is therefore considered the endpoint of the main reaction chain ^{4}He(2α,γ)^{12}C(α,γ)^{16}O(α,γ)^{20}Ne and determines, together with the rate of ^{12}C(α,γ)^{16}O, the ^{16}O abundance at the ignition of the carbon burning phase in late stellar evolution. The inverse reaction ^{20}Ne(γ,α)^{16}O is of importance in the subsequent neon burning phase which takes place at higher temperature ($>$1 GK) [1].

The low-energy reaction cross section is characterized by a number of different reaction components including the tails of resonant states above the α threshold at 4.730 MeV in ^{20}Ne, as shown in Fig. 1, and nonresonant contributions. Only natural parity states can be populated and will contribute to the resonance terms. At stellar energies the reaction is dominated by the nonresonant capture process while at higher energies the reaction can occur through resonant capture by way of several resonances. The lowest possible resonance contributions are due to the two narrow states at $E_x = 5.62$ MeV ($J^\pi = 3^-$) and $E_x = 5.79$ MeV ($J^\pi = 1^-$). The nonresonant contribution was analyzed theoretically by several authors [2–6] obtaining substantial differences in the *S*-factor extrapolation.

The theoretical calculations suggest that the main contribution to the nonresonant cross section comes from *s*-wave capture to the first excited state of ^{20}Ne. This transition is thought to interfere at higher energies with the $E_\alpha = 2.5$ MeV 0^+ resonant state and therefore it appears possible to obtain information on the nonresonant contribution from the interference region. This region was therefore studied by Hahn *et al.* [7] who measured the ^{16}O(α,γ)^{20}Ne reaction cross section at four off-resonance energies $E_{\text{c.m.}} = 1.77$, 2.2, 2.3, and 2.35 MeV, using the inverse kinematics technique, detecting ^{20}Ne recoils in coincidence with capture γ rays. From this measurement only upper limits were determined.

A study of the ^{16}O(α,γ)^{20}Ne reaction over a wide energy range was performed at the Dynamitron laboratory of the University of Stuttgart [8]. The reaction was studied with both a Ta$_2$O$_5$ solid target and a ^{16}O gas target RHINOCEROS [8]. The sensitivity reached between the top of the resonances and the lowest yield data was two and a half orders of magnitude. The resonance parameters from $E_\alpha = 1.1$ to 3.4 MeV were accurately determined but only upper limits were obtained for possible nonresonant contributions.

A further measurement of the ^{16}O(α,γ)^{20}Ne reaction was performed at the same laboratory [9]. This measurement was done with the gas target setup used in Ref. [8], upgraded with an active bismuth germanate (BGO) shield for the germanium detectors to lower the background induced by cosmic rays (see Sec. II). The reaction was measured from $E_\alpha = 1.1$ to 3.4 MeV reaching a sensitivity of more than four orders of magnitude. The experiment and results are described in Ref. [9].

The resultant yield curve, shown in Fig. 4.23 of Ref. [9] represents, potentially, the best data available for a thorough *R*-Matrix analysis of this reaction. Further, ^{16}O(α,α)^{16}O was measured concurrently in the same experimental setup allowing a simultaneous *R*-matrix analysis of both reactions channels. Unfortunately, the numerical values for the yield curve were not reported so that a digital scan of Fig. 4.23 was required to extract the data. The yield curve for the scanned data is shown in Fig. 2. Note that in Fig. 2 the three lowest yield points near $E_\alpha = 1.5$ MeV are shown as upper limits whereas in Fig. 4.23 [9], they are shown with associated error bars. This is discussed in Sec. II.

Moreover, in Ref. [9] there are some indications that the width of the 1.3 MeV 1^- resonance ($E_x = 5.788$ MeV) is considerably larger than previously measured [10], indicating a substantial increase in the value of the extrapolated *S*-factor data toward the stellar energy range. The overall detection efficiency for the gas target data of Ref. [9] relied on Monte Carlo simulations of the experimental setup. The Monte Carlo results were tested only at low γ energies using calibrated

---

[*] rdeboer1@nd.edu

[†] Formerly Institut für Strahlenphysik, University of Stuttgart.

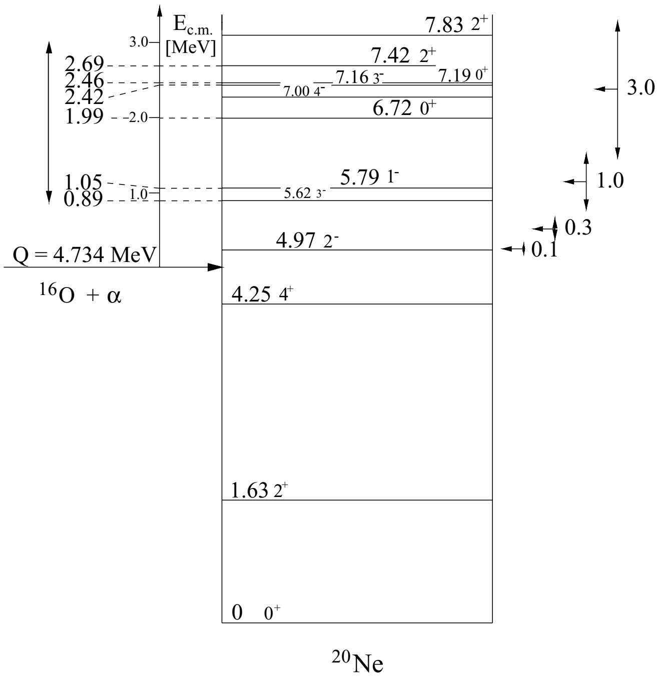

FIG. 1. Level scheme of ^{20}Ne. The natural parity α unbound states contribute as resonances to the ^{16}O(α,γ)^{20}Ne reaction rate. The Gamow energy range for this reaction at fixed stellar temperatures in GK is indicated at the right-hand side.

sources. Hence, absolute efficiency calibrations are desirable for the higher energies.

A new measurement of the ^{16}O(α,γ)^{20}Ne reaction was performed at the Nuclear Science Laboratory of the University of Notre Dame using a solid target approach. In this experiment the emphasis was first on the measurement of the cross section of the 0^+ resonance at $E_\alpha = 2.5$ MeV to establish an absolute calibration for the overall detection efficiency for the gas target data of Ref. [9], and second on the investigation of the width of the 1^- resonance at $E_\alpha = 1.3$ MeV with the goal of comparing it to the gas target data. With the new solid target data, it has been possible to normalize the previous gas target data (see Sec. IV) and thus obtain absolute yields that have been further analyzed using the R-matrix theory (see Sec. V).

A short summary of the previous gas target experiment and the data analysis procedure is presented in Sec. II. Extensive details can be found in Ref. [9].

II. A BRIEF SUMMARY OF THE GAS TARGET EXPERIMENT OF REF. [9]

The measurement of the ^{16}O(α,γ)^{20}Ne reaction was performed at the Dynamitron accelerator laboratory of the University of Stuttgart, Germany. The extended windowless recirculating gas target RHINOCEROS [9,11] was used for mapping the excitation curve. For the measurement of the γ yield, two high-resolution 100% geranium (Ge) detectors were mounted at angles of ±90° with respect to the beam direction. The close configuration resulted in a large acceptance angle from 10° to 170°, and considerable Doppler broadening of the γ lines. Modular ring-shaped BGO detectors surrounding the Ge crystals served as active shielding. The dependence of the γ detection efficiency for the Ge detector was determined with calibrated γ sources (^{60}Co and ^{226}Ra) at different positions along the beam axis in the target chamber. These low-energy efficiency measurements were compared with Monte Carlo efficiency simulations of the setup using the code GEANT 3.21 [12] and showed excellent agreement. The efficiency calculations at higher energies were not tested. Full experimental details are presented in Ref. [9].

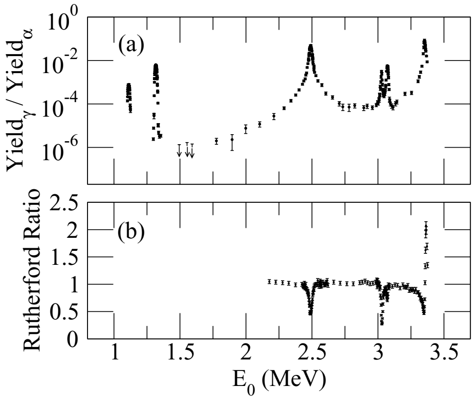

FIG. 2. The upper figure (a) displays the γ yield for the transition to the first excited state in ^{16}O(α,γ)^{20}Ne divided by the yield in the 90° particle detector, covering the energy range between $E_0 = 1.1$ MeV and 3.4 MeV (where E_0 is the energy in the laboratory frame as measured in the center of the gas target) scanned from Fig. 4.23 of Ref. [9]. The arrows mark data points which resemble 2σ upper limits for the reaction yield. The yield curve is characterized by several narrow resonances and two overlapping broad 0^+ resonances at $E_\alpha = 2.5$ and 3.1 MeV. The large range in yield of five orders of magnitude was obtained thanks to the gas target system RHINOCEROS [8]. A simple point to point yield to cross-section conversion was not possible for the data shown, prompting a follow up measurement at Notre Dame (see Sec. IV). The lower figure (b) shows the α yield divided by the theoretical Rutherford cross section in the 90° particle detector from Fig. 4.19 of Ref. [9] above $E_\alpha = 2$ MeV where deviation from Rutherford scattering was observed.

The resonance to first excited state ($R \rightarrow 1$) excitation curve of ^{16}O(α,γ)^{20}Ne was measured in the energy range between $E_\alpha = 1.1$ and 3.4 MeV and is shown in Fig. 2. The ^{16}O(α,γ)^{20}Ne yield at each energy was determined by Monte Carlo analysis of the observed line shape for each γ transition including the corrections for detector efficiency, extended target geometry, energy loss, detector geometry, and angular distribution. Only upper limits could be determined for the yield for the direct transition to the ground state. A typical spectrum is shown in Fig. 3.

The observed transition yield between resonances is very low. Figure 4, taken from Ref. [9], shows the observed spectrum at $E_\alpha = 1.59$ MeV. The cross section is too low to determine reliable yield values. For this reason, the data point at $E_\alpha = 1.59$ MeV as well as two other nearby data points with similar yield, were designated as upper limits (see Fig. 2). Removing these data points from the R-matrix fit described in the following had a minimal effect ($\Delta\chi^2 < 3\%$) since the reported error bars were quite large.

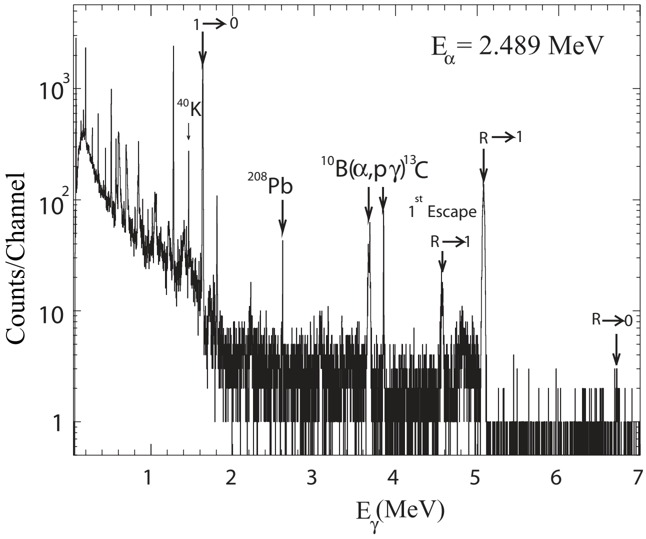

FIG. 3. The ^{16}O(α,γ)^{20}Ne yield measured at an energy of 2.489 MeV after accumulating 0.32 C of charge using the gas target system RHINOCEROS [8]. The primary transitions to the ground state and the first excited state are clearly visible (with permission [9]).

Details of this analysis can be found in Ref. [9]. Interpreting the data in terms of reaction contributions requires a detailed *R*-matrix analysis. This analysis will be discussed in Sec. V.

III. THE PRESENT SOLID TARGET EXPERIMENT

A. The experimental setup

To determine the width of the 1.3 MeV resonance and to provide a normalization for the gas target data, measurements with solid ^{16}O targets were carried out at the Nuclear Science Laboratory at the University of Notre Dame, using the 3.7 MV KN Van de Graaff accelerator. The accelerator delivered an α beam up to 150 μA. The beam was wobbled to produce a homogeneous beam spot size of 1.6 × 1.0 cm on the target. To reduce carbon deposition, a liquid nitrogen cooled copper tube was mounted in front of the target. The target was mounted on a water-cooled brass target holder. To measure the charge deposited on the target, the target chamber was electrically isolated and a bias voltage of −300 V was applied to the cold finger to repulse secondary electrons on the target. A detailed description of the experimental setup can be found in Ref. [13].

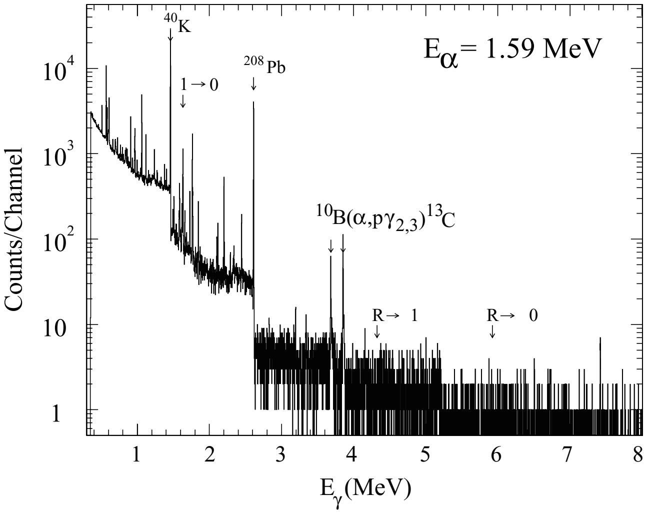

FIG. 4. The ^{16}O(α,γ)^{20}Ne yield measured at an energy of 1.59 MeV after 34.3 C of accumulated charge using the gas target system RHINOCEROS [8]. The primary transitions to the ground state and the first excited state are very weak. For the present analysis a 2σ upper limit has been determined for the yield at these energies. These upper limits are shown in Fig. 2 (with permission [9]).

The solid targets were produced by anodizing a 0.25 mm thick Ta backing using 99.999% enriched ^{16}O water [14]. Typical thickness of the tantalum-oxide, Ta_2O_5, layer was around 20 μg/cm^2 corresponding to 10 keV energy loss for $E_\alpha = 2.5$ MeV.

The experiment was divided into two phases. In the first phase, the width of the $E_\alpha = 1.3$ MeV resonance was measured. With a typical beam current of $\approx$100 μA, the Ta_2O_5 targets remained stable over 3 C of charge accumulation. The γ detection system consisted of four NaI(Tl) detectors and a high-purity germanium clover detector, with the clover operated in add-back mode. The clover detector was placed at a distance of 0.65 cm from the target, and at 45° with respect to the beam direction. Details of the detector arrangement were described earlier [13].

The 1.3 MeV resonance decays primarily to the first excited state [15] with a γ transition of 4.156 MeV ($R \rightarrow 1^{st}$). The secondary transition of $E_\gamma = 1.634$ MeV proceeds to the ground state ($1^{st} \rightarrow 0$). The second branch decays directly to the ground state ($R \rightarrow 0$) with $E_\gamma = 5.79$ MeV.

For the measurement of the total width, the detectors were operated in coincidence mode with the NaI(Tl)'s observing the high-energy primary γ-ray decay of the 1.3 MeV resonance state, and the clover observing the secondary 1.634 MeV γ-ray transition from the first excited state to the ground state. The trigger for the data acquisition was an event in the clover detector with the energy above the threshold of approximately 0.1 MeV. This created a coincidence requirement for the NaI(Tl) detectors, as their signals would only be acquired if they came in coincidence with a clover signal. An example spectrum is shown in Fig. 5.

The coincidence method significantly decreased the background with a corresponding increase in the signal-to-noise ratio. The coincidence yield was used exclusively for the measurement of the resonance width.

In the second phase of the experiment, the yield curve for the $E_\alpha = 2.5$ MeV resonance was measured to determine absolute normalization of the gas target data of Ref. [9]. Only the primary resonant decay to the first excited state was used in this measurement because the background reaction ^{17}O($\alpha, n - \gamma$) contributed significantly to the yield of the 1.634 MeV secondary γ transition.

The solid target thickness was chosen to be identical to the thickness of the extended gas target [i.e. $\Delta E(E_\alpha = 2.5\text{ MeV}) = 10$ keV]. At this higher α-beam energy, the targets deteriorated much faster due to the high beam power. The beam was therefore de-focused and wobbled across the target, and the current was limited to 30 μA. The targets

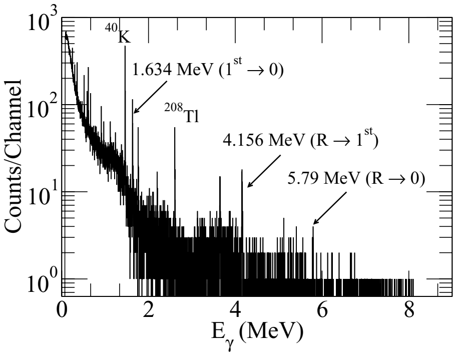

FIG. 5. Example γ spectrum for the ^{16}O(α,γ)^{20}Ne reaction taken at Notre Dame after 3 C of charge deposition. This spectrum is the sum of the four germanium crystals making up the clover detector at an α beam energy of 1.322 MeV on top of the narrow 1^- resonance. Transitions from resonance to ground state ($R \rightarrow 0$), resonance to first excited state ($R \rightarrow 1^{\text{st}}$), and first excited state to ground state ($1^{\text{st}} \rightarrow 0$) are clearly visible.

were changed after 0.3 C of collected charge to ensure target stability. The targets did not show any significant signs of deterioration. During this phase, data were taken only with the clover detector in "singles" mode. In addition, the isotropic decay of this resonance allowed the placement of the Ge clover detector in close geometry at 0° with respect to the beam direction to increase the overall statistics (see Fig. 6 for an example spectrum). The absolute "singles" efficiency for the clover detector was determined using a ^{60}Co source and the well-known ^{27}Al(p,γ)^{28}Si resonances at $E_p = 0.679$ and 0.992 MeV. Relative values for the resonance strengths were taken from Ref. [16] and were scaled to the $E_p = 0.992$ MeV resonance strength given by Ref. [17].

B. The 1.3 MeV resonance in ^{16}O(α,γ)^{20}Ne

The 1^- level at $E_\alpha = 1.3$ MeV ($E_x = 5.788$ MeV) decays by $E1$ transitions to the ground state and the first excited state at $E_x = 1.63$ MeV. The coincidence yield curve for the cascade transition for the $E_\alpha = 1.3$ MeV resonance is shown in Fig. 7 together with the best fit of the front edge of the resonance scan. The fitted curve is obtained from the expression (Eq. (5.44) in Ref. [18])

$$Y(E) = K \int_{E-\Delta}^{E} \int_{0}^{\infty} \frac{\sigma_{bw}(E^{'})}{\epsilon(E^{'})} g(E^{'}, E)\, dE^{'} dE, \qquad (1)$$

where K is a normalization constant, Δ is the target thickness, ϵ is the effective stopping power of the α beam in the Ta$_2$O$_5$ target (stopping power values were taken from SRIM [19]), $g(E^{'}, E)$ is the Gaussian energy distribution of the incident α-beam particles, and σ_{bw} is the Breit-Wigner cross section for an isolated broad resonance (Eq. (4.59) in Ref. [18]).

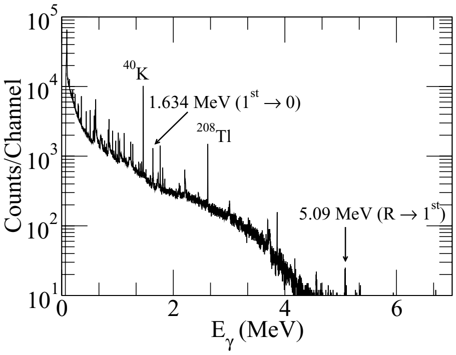

FIG. 6. Example γ spectrum for the ^{16}O(α,γ)^{20}Ne reaction taken at Notre Dame after 0.3 C of charge deposition. This spectrum is the sum of the four germanium crystals of the clover detector at an α beam energy of 2.430 MeV near the top of the broad 0^+ resonance. At this energy significant background from ^{17}O($\alpha, n-\gamma$) contaminated the 1.634 MeV first excited state to ground state transition photopeak so the coincidence method could not be used. Therefore only the primary transition peak at 5.09 MeV was used for the yield measurement.

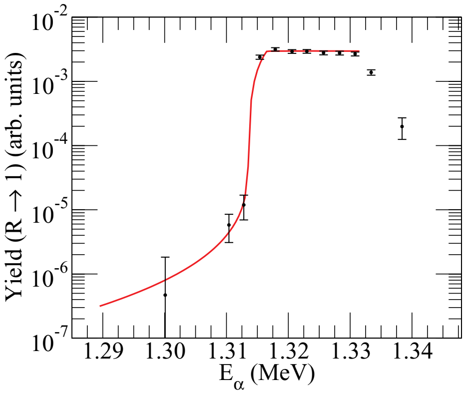

FIG. 7. (Color online) Scan of the ^{16}O(α,γ)^{20}Ne resonance at $E_\alpha = 1.3$ MeV. The black dots are the measured yield, while the red solid line represents the "best fit" of the front edge of the resonance using Eq. (1).

The α width was determined by the fit of the thick target resonance curve to a Breit-Wigner function. A value of $\Gamma_\alpha = 45(15)$ eV was obtained, which is in agreement with the previous result of the elastic scattering experiment by Ref. [10], $\Gamma_\alpha = 28(3)$ eV.

The absolute resonance strength $\omega\gamma$ of the $E_\alpha = 1.3$ MeV resonance was determined using the second detection arrangement with a clover detector mounted at 0° with respect to the beam direction. Angular distribution and summing corrections were applied and a value of $\omega\gamma = 14(2)$ meV was obtained which is lower than the value quoted in more recent works [7–9] but in agreement with the results of older measurements [20,21] (see Table I). The branching ratios for the γ decay of the 5.788 MeV level to the ground state and first excited state in ^{20}Ne were determined to be 16(5)% and 84(5)%, respectively (see Table I), which is in agreement with previous works [7–9,20].

The strengths of the $E_\alpha = 1.1$ and 2.5 MeV resonances were also determined in a similar manner, and values for $\omega\gamma$ were found to be 1.8(3) and 85(9) meV, respectively. The strength of the $E_\alpha = 1.1$ MeV resonance is found to be in good agreement with previous measurements [8,9,20,21] and that obtained for the $E_\alpha = 2.5$ MeV resonance is in excellent agreement with the result of the R-matrix analysis described in the following (see Sec. V). Table I gives a comparison of all previous strength, width, and branching ratio measurements

TABLE I. Parameters for the resonances at $E_\alpha = 1.1$ MeV, $J^\pi = 3^-$ (top) and 1.3 MeV, $J^\pi = 1^-$ (bottom). The last column indicates the values that were adopted in the R-matrix calculation (see Sec. V). The adopted values are determined by weighted averages and the uncertainties are the larger of the internal and external uncertainties (see, e.g., Refs. [22,23]). Note that energies are given in the laboratory frame while all widths and strengths are given in the center-of-mass frame.

	This work	Van der Leun [20]	Toevs [21]	MacArthur [10]	Hahn [7]	Knee [8]	Mayer [9]	Adopted value
E_α (keV)	1 113.7(10)	1 116(4)				1 113(3)	1 113(3)	1 114(1)
$\omega\gamma$ (meV)	1.8(4)	1.4(4)	1.5(3)[a]			1.9(3)	1.8(3)	1.7(2)
Γ (eV)		2.6×10^{-3}					$\leqslant 500$	2.6×10^{-3}
$BR(R \rightarrow 1)$ (%)						89.8(11)	91.6(20)	90.2(10)
$BR(R \rightarrow 0)$ (%)						6.9(14)	3.5(6)	4.0(12)
E_α (keV)	1 314.8(15)	1 319(3)		1 317.4(22)		1 317(3)	1 317(3)	1 316.1(22)
$\omega\gamma$ (meV)	14(2)	12(3)	14.6(29)[a]		19.7(41)	21.8(29)	19(3)	16.3(16)
Γ (eV)	45(15)	>13		28(3)			300(100)	28(3)
$BR(R \rightarrow 1)$ (%)	84(5)	82(5)			81(4)	76.3(38)	72.5(20)	76(2)
$BR(R \rightarrow 0)$ (%)	16(5)	18(5)			19(4)	23.7(38)	25.5(20)	23(2)

[a] Ref. [21] reports $\omega\gamma_{\rm lab} = 1.9(4)$ and 18.2(36) meV for the $E_\alpha = 1.1$ and 1.3 MeV resonances, respectively. Here $\omega\gamma_{\rm lab} = \omega\gamma_{\rm c.m.}(\frac{m+M}{M})$, where M is the mass of the target particle and m is the mass of the projectile.

for the two lowest-energy resonances. The values adopted are weighted averages of all measurements including those made here.

IV. THE 2.5 MeV RESONANCE: REACTION CROSS SECTION OF ^{16}O(α,γ)^{20}Ne

The data from Ref. [9] shown in Fig. 2 represent the yield of the primary transition to the first excited state ($R \rightarrow 1$) γ ray in the germanium detectors normalized to the yield of the elastically scattered α particles at 90°

$$Y_{\rm gas}(E_0) = \frac{Y_\gamma}{Y_\alpha(E_0)} = \frac{N_\gamma}{Y_\alpha(E_0)} \int_{L_{\rm targ}} \sigma(E[z])\eta(z, E_\gamma, W[\theta])\rho(z)\,dz, \quad (2)$$

where $\rho(z)$ is the density profile of the gas target and η is the efficiency profile of the germanium detectors that depends on the energy of the γ ray and on the angular distribution $W(\theta)$. The efficiencies for the high γ energies of the ^{16}O(α,γ)^{20}Ne primary transitions relied on GEANT simulations [9]. This results in considerable uncertainty in the initial data set.

For the present experiment, the yields for the $E_\alpha =$ 2.5 MeV resonance were obtained from the net area (I) of the γ peak for the primary transition

$$Y(E_b) = \frac{Ie}{Q\eta} = \int_{E_b-\Delta}^{E_b} \frac{\sigma(E)}{\epsilon(E)}\,dE, \quad (3)$$

where Q is the collected charge, e is the charge of the electron, Δ is the target thickness, ϵ is the effective stopping power [19], and η is the detection efficiency. This yield curve is shown in Fig. 8 in comparison to the gas target data. The latter is normalized to the solid target data to allow the shape comparison. Since the stopping power can be considered constant over the target thickness, the integrated cross section can be obtained from Eq. (3)

$$\int_{E_\alpha-\Delta}^{E_b} \sigma(E)\,dE = Y(E_b)\frac{\epsilon}{\eta}. \quad (4)$$

Several tests have been done to determine the best suited energy range for the normalization of the two data sets. The integrated cross section weighted with the efficiency and density profile of the target in Eq. (2) was numerically calculated at the $E_\alpha = 2.5$ MeV resonance. For the calculation, the literature values of the resonance parameters [15] were adopted and an efficiency profile, obtained by simulation through a GEANT 3.21 Monte Carlo code [12] of the gas target apparatus, was assumed. This quantity was compared to the integrated cross section, assuming a constant efficiency and density profile along the target thickness, as in the solid target experiment. The ratio of the two was then calculated as a

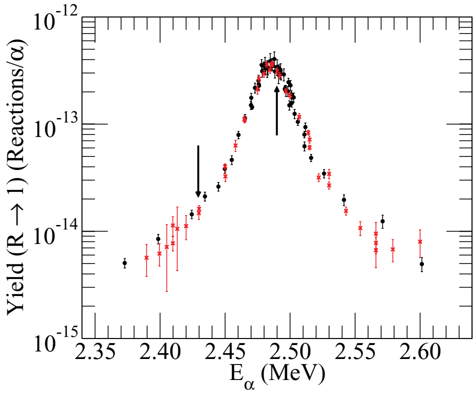

FIG. 8. (Color online) The yield curve for the ^{16}O(α,γ)^{20}Ne reaction over the $E_\alpha = 2.5$ MeV resonance. The red crosses are the data taken at Notre Dame, while the black dots are the Stuttgart gas target data normalized to the Notre Dame data. The black arrows mark the energies ($E_\alpha = 2.430$ and 2.490 MeV) where the normalization was made.

function of the impinging α energy

$$R(E_b) = \frac{\int_{L_{\rm targ}} \sigma_{\rm bw}(E[z])\eta(z)\rho(z)\,dz}{\int_{L_{\rm targ}} \sigma_{\rm bw}(E[z])\,dz}, \qquad (5)$$

where $L_{\rm targ}$ is the gas target length. It was found that in the case of a broad resonance such as the $E_\alpha = 2.5$ MeV, the effects of an extended gas target (density and efficiency profiles along the target length) can be considered almost negligible. The normalization was made at two specific energies $E_\alpha = 2.430$ and 2.490 MeV where the difference in $R(E_b)$ from unity was calculated to be smaller than 0.5%. Therefore Eq. (2) can be written as

$$\begin{aligned} Y_{\rm gas}(E_0) &= \frac{N_\gamma}{Y_\alpha(E_0)}\eta(E_b)\rho\int_{L_{\rm targ}} \\ \sigma(E[z])\,dz &= \frac{N_\gamma}{Y_\alpha(E_0)}\frac{\eta(E_b)}{\epsilon(E_b)}\int_{E_b-\Delta}^{E_b}\sigma(E)\,dE. \qquad (6) \end{aligned}$$

The last integral term can be obtained from the solid target measurement at the same incident beam energy [Eq. (4)]. Since the solid targets deteriorated quickly, different targets were used for the same normalization energy and the difference in target thickness was at maximum 1 keV, corresponding to a maximum uncertainty of 4% in the normalization procedure. Finally the normalization of the Stuttgart data to the Notre Dame data could be obtained by inverting Eq. (6). This operation was performed at both 2.430 and 2.490 MeV and resulted in identical values within the experimental uncertainty of the Notre Dame measurements (10%). The uncertainty includes, besides the statistical errors, the uncertainties of the absolute detection efficiency (7%), the absolute charge measurement (2%), the stopping power taken from SRIM [19] (3%) and the target thickness effect (4%). Since the normalization was performed only at the $E_\alpha = 2.5$ MeV resonance, the energy-dependent quantities had to be evaluated and included in the overall normalization procedure. The Monte Carlo simulation code was used to evaluate the energy dependence of the gas target efficiency and the effects of angular distribution on the measured gas target yield. Due to the large solid angle subtended by the germanium detectors and the extended target, the angular distribution effects were almost negligible, except for the 3^- resonance at 3.0 MeV that had to be corrected by 10%. The normalized yield for the gas target data, as defined in Eq. (3) where ϵ is the stopping power in the oxygen gas target, is shown in Fig. 9.

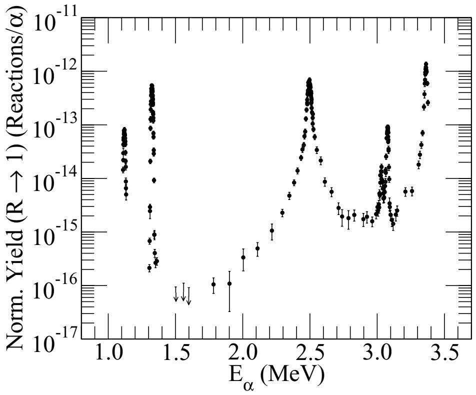

FIG. 9. The figure shows the yield ratio in Fig. 2 corrected for the normalization to the 90° particle detector. Absolute normalization was obtained by normalizing the gas target data to the Notre Dame solid target data at the $E_\alpha = 2.5$ MeV resonance as shown in Fig. 8. Here the yield curve ($\int_{E_b-\Delta}^{E_b}\frac{\sigma(E)}{\epsilon(E)}dE$) contains target and beam effects, which will be simulated in the R-matrix analysis in Sec. V A.

V. *R*-MATRIX ANALYSIS

The multichannel multilevel R-matrix code AZURE [24] was used for a simultaneous analysis of the ^{16}O$(\alpha,\gamma)^{20}$Ne ($R \to 1$) normalized yield and the 90° elastic scattering data. For a detailed description of the underlying R-matrix formalism and further details on the AZURE code, see Refs. [24,25].

A. *R*-Matrix: resonance contributions

Six resonances were observed in the gas target excitation curves corresponding to known states in ^{20}Ne [15]. Of the six observed resonances only the two $J^\pi = 0^+$ resonances at $E_\alpha = 2.490$ and 3.069 MeV display appreciable interference, with the "best fit" obtained with opposing interference signs. The remaining contributions include a single narrow and isolated $J^\pi = 1^-$ resonance at $E_\alpha = 1.3\,174$ MeV, two $J^\pi = 3^-$ resonances at $E_\alpha = 1.116$ and $3.0\,359$ MeV and a single $J^\pi = 2^+$ resonance at $E_\alpha = 3.359$ MeV. A scan of the R-matrix radius parameter, as a function of the χ^2 of the fit, found only a weak dependence. A value of 5.5 fm was used for all calculations. Lowest-order orbital angular momentum values were found to dominate for all fitted resonances. A density of 3.6×10^{17} O$_2$ particles/cm^2 was used for the gas target (calculated from information on the gas target given in Sec. 4.3.1 of Ref. [9]).

Beam effects in both the (α,γ) and (α,α) data sets were modeled with the convolution and target averaging routines of AZURE [26]. The convolution model uses two back-to-back Gaussians to simulate the beam's energy distribution (as described in Ref. [26]) and possible straggling effects. For both data sets a value of $\sigma = 2$ keV was taken as the energy resolution of both Gaussians (no appreciable straggling effects were found) at the center of the gas target. The value for the energy resolution was determined independently from the experimental setup [9] and from a χ^2 minimization of the convolution parameters.

The resonance parameters of Ref. [15] (see Table II) were found to be good starting parameters for the R-matrix analysis. Figure 10 shows the R-matrix fit of the ^{16}O$(\alpha,\gamma)^{20}$Ne ($R \to 1$) yield curve given in Fig. 9. The fit was performed simultaneously with the fit of the scattering data shown in Fig. 2. Taking only the resonances into account results in a clear deviation of the *resonance only* fit from the (α,γ) data in the nonresonant regions of the yield curve as shown by the dashed line in Fig. 10. Nonresonant contributions such as external capture or tails from higher-energy resonances have to be taken into account to improve the fit in these regions.

The extremely narrow 3^- and 1^- resonances at $E_\alpha = 1.1$ and 1.3 MeV, respectively, were included in the R-matrix

TABLE II. R-matrix analysis results. Uncertainties for center-of-mass Γ_{total} and $\omega\gamma_{(\alpha,\gamma)}$ of the present work are given in the form (statistical + systematic). The statistical errors are derived from the χ^2 error analysis while the systematic error comes from the 10% uncertainty in the yield normalization (see Sec. IV). The uncertainties on the level energies are of the same form but the systematic uncertainty comes from the uncertainty in the energy calibration of the Stuttgart experiment (2 keV). Interference signs were taken as positive as the default for the R-matrix fit parameters. The resonances at $E_\alpha = 2.490$ MeV and 3.359 MeV were found to require negative interference signs to produce the "best fit."

This work					Compilation [15]		
E_α (MeV)	E_x (MeV)	J^π	Γ_{total} (keV)[a]	$\omega\gamma_{(\alpha,\gamma)}$ (meV)[b]	E_x (MeV)	Γ_{total} (keV)	$\omega\gamma_{(\alpha,\gamma)}$ (meV)
2.490	6.7263(5 + 20)	0^+	17.8(14)	85(3 + 9)	6.726(6)	19.0(9)	71(12)
3.029	7.1569(2 + 20)	3^-	6.8(15)	11(2 + 1)[c]	7.1563(5)	8.2(3)	11.3(11)
3.072	7.1918(3 + 20)	0^+	2.7(6)	5.8(4 + 6)	7.189(3)	3.4(2)	4.4(8)
3.359	7.4214(5 + 20)	2^+	9.0(13)	132(11 + 13)[d]	7.421(1)	8	146(19)

[a] $\Gamma_{\text{total}} \approx \Gamma_\alpha$.

[b] $\omega\gamma_{(\alpha,\gamma)} \approx (2J+1)\Gamma_\gamma$.

[c] $\omega\gamma_{(\alpha,\gamma)}(3^- \rightarrow 1^{\text{st}}$ excited state$) = 1.0(2 + 1)$ assuming BR$(3^- \rightarrow 1^{\text{st}}$ excited state$) = 9\%$ [9].

[d] $\omega\gamma_{(\alpha,\gamma)}(2^+ \rightarrow 1^{\text{st}}$ excited state$) = 117(10 + 12)$ assuming BR$(2^+ \rightarrow 1^{\text{st}}$ excited state$) = 88.4\%$ [9].

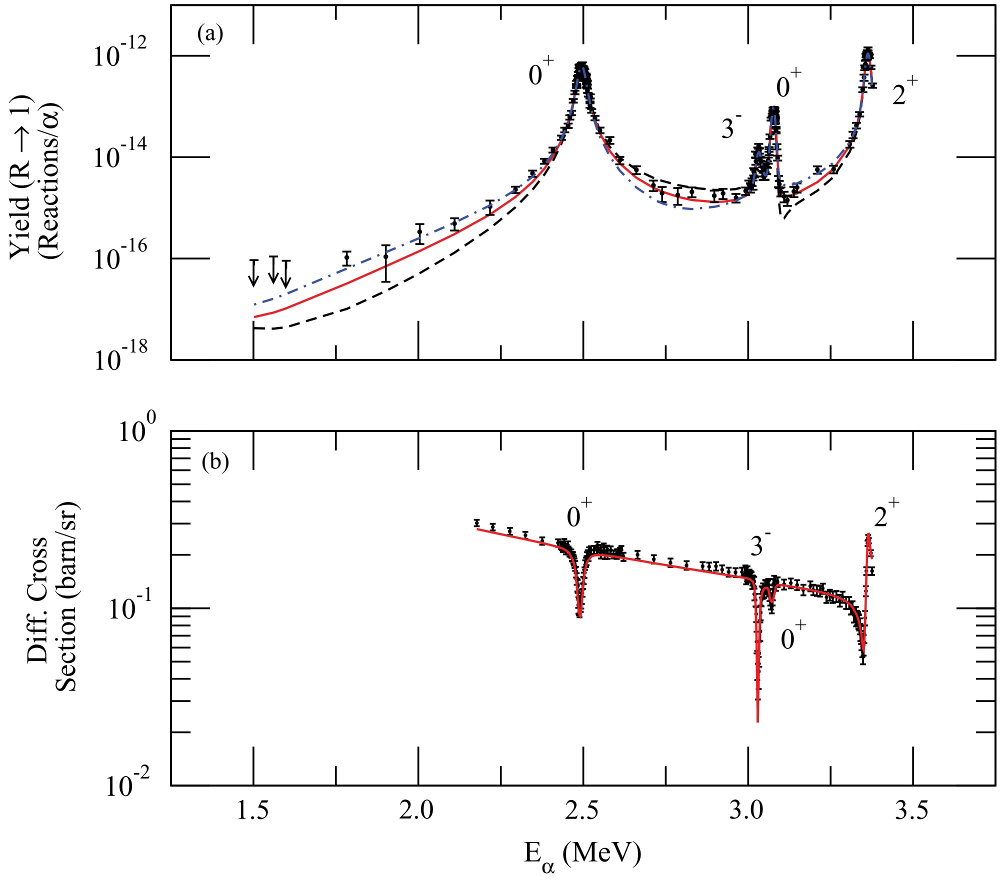

FIG. 10. (Color online) The ^{16}O(α,γ)^{20}Ne [151 data points, top (a)] and ^{16}O(α,α)^{16}O data [166 data points, bottom (b)] [9] are shown as black points with error bars. The (α,γ) fit, including only resonance terms and target effect simulation, is shown by the black dashed curve and clearly deviates significantly from the observed data ($\chi^2_{(\alpha,\gamma)}/N = 3.24$, $\chi^2_{(\alpha\alpha)}/N = 1.02$). The R-matrix "best fit" including also nonresonant s and d wave $E2$ EC components is shown as a solid red line (color online) and demonstrates a substantial improvement in the description of the experimental data ($\chi^2_{(\alpha,\gamma)}/N = 2.22$, $\chi^2_{(\alpha\alpha)}/N = 1.05$). Also shown in dot-dashed blue is the other interference possibility for the large 0^+ resonance at $E_\alpha = 2.49$ MeV ($\chi^2_{(\alpha,\gamma)}/N = 2.72$ and $\chi^2_{(\alpha\alpha)}/N = 1.11$). The fit matches the data points on the low energy side of the large 0^+ resonance but significantly deviates from the data in other regions. The (α,α) fit is only shown for the "best fit" case since only small deviations were observed for the other fits.

calculation as fixed poles using the adopted resonance parameter given in Table I. The analysis for the two resonances was done independently and is discussed in Sec. III B.

B. External capture contribution

A hard sphere external capture (EC) component was included in the R-matrix calculation [24]. The s and d wave $E2$ EC contributions were included since $E2$ should dominate [6].

For spin-zero EC, the s and d partial waves have total angular momentum $J_i = 0, 2$ with orbital angular momentum $l_i = 0, 2$, respectively. The orbital and spin angular momenta of the first excited state of ^{20}Ne are $l_f = 2$ and $s_f = 0$, respectively. The strength of the EC is given in terms of the asymptotic normalization coefficient (ANC) (see, e.g., Refs. [27,28]).

The "best fit" shown in Fig. 10 yields the value of ANC$= 2\,500$ $(800 + 250)$ fm$^{-1/2}$ (statistical + systematic), consistent with the spectroscopic factor (corresponding to an ANC $= 3\,400(700)$ fm$^{-1/2}$) reported by Ref. [29]. Significant interference occurs between the EC and the large $E_\alpha = 2.490$ MeV 0^+ resonance in the nearby regions. Excellent agreement is found over the entire energy range of both data sets.

For a multivariable fit the confidence level is characterized by $\chi^2 \leqslant \chi^2_{\mathrm{min}} + \Delta\chi^2$ [30]. For this analysis 13 free fit parameters (four resonance energies, eight partial widths, one ANC) were used corresponding to a value of $\Delta\chi^2 \sim 15$ for a $\sim$70% confidence level. A 10% systematic uncertainty is present from the normalization process (see Sec. IV). Since the systematic uncertainty from the normalization only effects the relative scaling of the yield data only $\omega\gamma$ and the ANC are significantly affected.

C. Background poles

Nineteen levels above the experimental energy region have been reported including the critical resonance parameters Γ_{total}, $\omega\gamma$, and branching ratio values (BR) [15]. These resonances were added as individual background poles with their widths and energies fixed. These higher-energy resonances had no significant effect on the quality of the fit ($\Delta\chi^2 < 2\%$). Different interference combinations were also investigated but had no significant effect. However, the tails of these higher-energy resonances resulted in a slight decrease in the amplitude of the EC necessary to produce the same fit. The effect on the ANC is less than 1σ but it is significant. An example calculation is shown in Fig. 11.

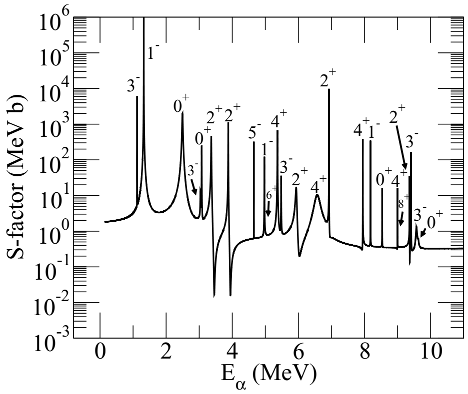

FIG. 11. An example R-matrix calculation of the S factor including all known resonances at higher energy [15]. None of the higher-energy resonances were broad enough to have a significant effect ($\Delta\chi^2 < 2\%$) on the fit in the experimental data region. The addition of known background poles did decrease the ANC needed to produce the same fit reducing the ANC from $3\,000$ fm$^{-1/2}$ to 2500 fm$^{-1/2}$. This had no significant effect on the χ^2 of the fit because the tails of the background poles and the EC have a sufficiently similar energy dependence in the experimental region.

Other possible physical background poles are the giant quadrupole resonances (GQR's) at energies ranging from $E_x = 11$ to 25 MeV [31]. A background pole representing the strength of all GQR's was placed at $E_x = 24$ MeV ($J^\pi = 2^+$). Estimates of Γ_{total} of the GQR's are well established (see, e.g., Ref. [32]) and are of order MeV (a value of $\Gamma_{\mathrm{total}} = \Gamma_\alpha = 5.9$ MeV was used). Γ_γ for these resonances remain unmeasured as they are quite small compared to the particle widths. The "best fit" was obtained with $\Gamma_\gamma = 10$ eV, which is the right order of magnitude for a typical GQR strength [31]. With these widths, the contribution of the GQR's to the cross section in the Gamow window is negligible (see Fig. 12).

D. *S*-factor extrapolation

The EC is found to be the dominant contribution to the cross section at $E_{\mathrm{c.m.}} = 300$ keV and is enhanced by $\sim$10% through its interference with the broad 0^+ resonance at $E_\alpha = 2.490$ MeV. The S-factor calculated for the first excited state transition ($R \rightarrow 1$) was extrapolated using the "best fit" R-matrix parameters. The extrapolation is shown in Fig. 12.

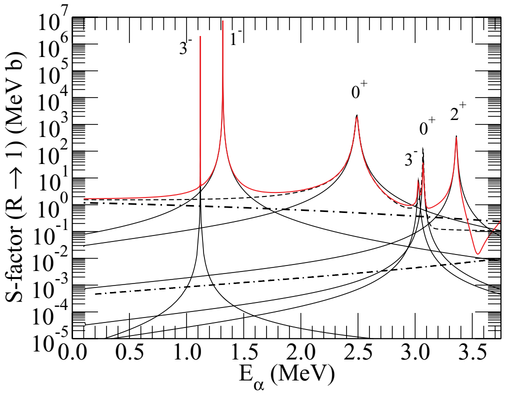

FIG. 12. (Color online) Shown in solid red is the S factor ($R \rightarrow 1$) curve extrapolated from the "best fit" of Fig. 10. In thin black lines are the contributions from individual resonances. The black dashed line represents the combined effects of EC and two 0^+ resonances that strongly interfere creating the major contribution to the $E_{\mathrm{c.m.}} =$ 300 keV S factor. The sum of all background pole contributions, including the GQR's, is given by the dot-dash-dash line.

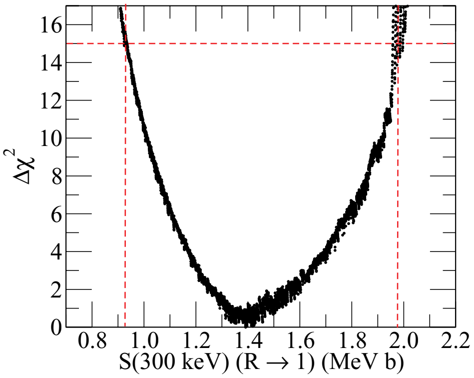

FIG. 13. (Color online) A scan of $S(300\,\text{keV})$ as it varies with the χ^2 of the R-matrix fit. A value of $\Delta\chi^2 = 15$ corresponds to a 70% confidence level and is shown by the intersecting red dashed lines. The "best fit" value for the S factor is found to be 1.4 MeV b with a statistical uncertainty of 0.6 MeV b and a systematic uncertainty of 0.2 MeV b resulting from the uncertainty in the overall yield curve normalization.

Background poles shown in Fig. 11 were also included at higher energies.

The fitted value for the ANC, 2500 fm$^{-1/2}$, corresponds to $S_{R\to 1}(300\,\text{keV}) = 1.4$ MeV b (see Fig. 13). For the EC, the branching ratio to the first excited state remains uncertain. Here we adopted a value for the branching ratio of 75(10)% to the first excited state and 25(10)% to the ground state based on the theoretical prediction and experimental upper limits of Refs. [6–9]. With this adopted branching ratio, the total S factor is $S(300\,\text{keV}) = 1.9$ MeV b.

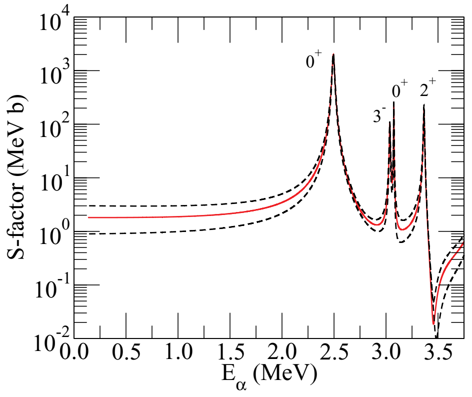

FIG. 14. (Color online) A calculation of the uncertainty in the (α,γ) S factor using the "best fit" R-matrix parameters from the fit shown in Fig. 10 (solid red line). The fit parameters obtained from the upper and lower 70% confidence points of the $S_{R\to 1}(300\,\text{keV})$ scan of Fig. 13 were used to calculate the upper and lower uncertainties in the S factor, which are shown by the black dashed lines. These upper and lower uncertainty curves were subsequently used to calculate the upper and lower bounds on the reaction rate. Note that the two lowest-energy resonances are not shown since their contribution to the rate was included separately as discussed in the text.

TABLE III. The $^{16}O(\alpha,\gamma)^{20}Ne$ reaction rate, calculated by numerical integration of the S-factor curve shown in Fig. 11.

T [GK]	Reaction rate [cm^3 mole^{-1} s^{-1}]		
	Lower bound	Base rate	Upper bound
0.10	3.17×10^{-27}	7.13×10^{-27}	1.11×10^{-26}
0.11	4.33×10^{-26}	9.74×10^{-26}	1.52×10^{-25}
0.12	4.38×10^{-25}	9.85×10^{-25}	1.53×10^{-24}
0.13	3.46×10^{-24}	7.80×10^{-24}	1.21×10^{-23}
0.14	2.24×10^{-23}	5.03×10^{-23}	7.83×10^{-23}
0.15	1.22×10^{-22}	2.74×10^{-22}	4.26×10^{-22}
0.16	5.74×10^{-22}	1.29×10^{-21}	2.01×10^{-21}
0.18	8.94×10^{-21}	2.01×10^{-20}	3.12×10^{-20}
0.2	1.07×10^{-19}	2.30×10^{-19}	3.53×10^{-19}
0.25	3.15×10^{-16}	4.21×10^{-16}	5.47×10^{-16}
0.3	2.37×10^{-13}	3.02×10^{-13}	3.79×10^{-13}
0.35	2.71×10^{-11}	3.38×10^{-11}	4.17×10^{-11}
0.4	9.39×10^{-10}	1.16×10^{-9}	1.41×10^{-9}
0.45	1.48×10^{-8}	1.81×10^{-8}	2.17×10^{-8}
0.5	1.36×10^{-7}	1.63×10^{-7}	1.95×10^{-7}
0.6	3.80×10^{-6}	4.51×10^{-6}	5.30×10^{-6}
0.7	4.15×10^{-5}	4.88×10^{-5}	5.67×10^{-5}
0.8	2.50×10^{-4}	2.93×10^{-4}	3.37×10^{-4}
0.9	1.01×10^{-3}	1.18×10^{-3}	1.35×10^{-3}
1	3.08×10^{-3}	3.56×10^{-3}	4.06×10^{-3}
1.25	2.22×10^{-2}	2.55×10^{-2}	2.90×10^{-2}
1.5	8.06×10^{-2}	9.21×10^{-2}	1.04×10^{-1}
1.75	1.97×10^{-1}	2.25×10^{-1}	2.53×10^{-1}
2	3.79×10^{-1}	4.32×10^{-1}	4.85×10^{-1}
2.5	9.26×10^{-1}	1.05×10^{0}	1.18×10^{0}
3	1.67×10^{0}	1.90×10^{0}	2.14×10^{0}
3.5	2.60×10^{0}	2.97×10^{0}	3.34×10^{0}
4	3.74×10^{0}	4.29×10^{0}	4.84×10^{0}
5	7.06×10^{0}	8.19×10^{0}	9.36×10^{0}
6	1.30×10^{1}	1.53×10^{1}	1.78×10^{1}
7	2.36×10^{1}	2.81×10^{1}	3.31×10^{1}
8	4.08×10^{1}	4.91×10^{1}	5.82×10^{1}
9	6.62×10^{1}	8.01×10^{1}	9.52×10^{1}
10	1.00×10^{2}	1.21×10^{2}	1.45×10^{2}

A scan of $S_{R\to 1}(300\,\text{keV})$ versus χ^2 is given in Fig. 13. The curve is nearly symmetric about the "best fit" value of 1.4 MeV b. A value of $\Delta\chi^2 \approx 15$ corresponds to a 70% confidence level which gives a value of 0.6 MeV b for the statistical uncertainty. Combining this with the systematic uncertainty from the normalization produces a total uncertainty of $(0.6 + 0.2)$ MeV b. Taking into account the adopted EC branching ratio gives a final value of $S(300\,\text{keV}) = 1.9(8 + 2)$ MeV b. The uncertainty in the S factor, found from the R-matrix fit, over the entire experimental region is shown in Fig. 14.

E. Reaction rate

An $^{16}O(\alpha,\gamma)^{20}Ne$ reaction rate calculation was performed by numerically integrating the extrapolated *total* S-factor curve spanning the energy range from $E_\alpha = 0.1$ to 10 MeV (see Fig. 11). The reaction rate was calculated between 0.1 and 10 GK (see Table III and Fig. 15). The calculation included

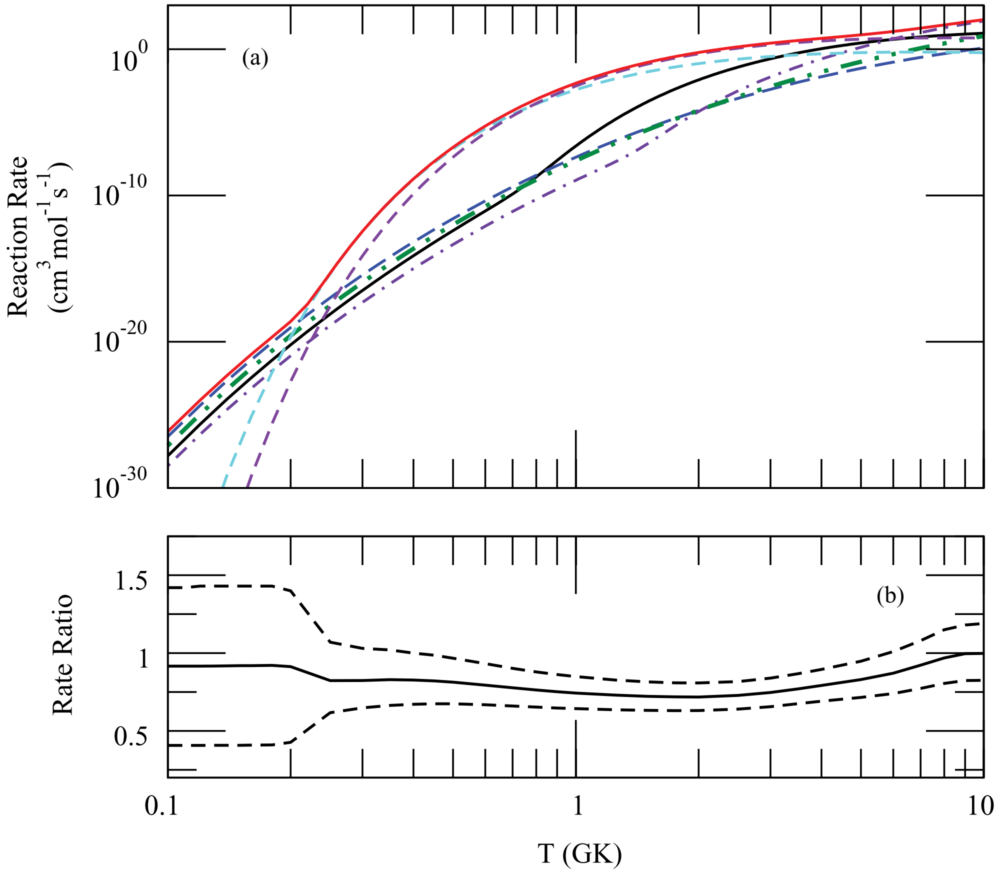

FIG. 15. (Color online) The upper figure (a) displays the total $^{16}O(\alpha,\gamma)^{20}Ne$ reaction rate calculated by numerical integration of the *S*-factor curve from Fig. 11, which is shown in solid red (color online). Also shown are the various reaction rate components discussed in the text. The EC contribution (dashed blue) is the most significant up to about 0.2 GK where the $E_x = 5.627\ 3^-$ (dashed cyan line) and the $E_x = 5.7877\ 1^-$ (dashed violet line) resonances quickly become dominant. These two resonances remain the main contributors to the rate up to approximately 5 GK where the sum of the higher-energy resonances (those in the experimental region (solid black) and higher (dashed-dotted indigo line)) finally become significant. The contribution from the GQR is also included (dashed-dot-dot green), but it should be noted that this is only an estimate since only approximations for its widths could be made due to the absence of experimental data. The lower plot (b) shows the ratio of the rate found in this work (solid black line) and its upper and lower bounds (black dashed lines) to that of the NACRE rate [33]. The upper and lower bounds on the rate were calculated using the upper and lower bounds on the *S*-factor curve from Fig. 14 and the uncertainties on the $\omega\gamma$ values and energies from Table I for the two lowest-energy resonances.

all resonances in the experimental region (see Table II and Fig. 10) and all of the known higher energy levels found in Ref. [15]. Because of the extremely narrow widths of the two lowest-lying resonances their contributions to the rate were included using the formula for isolated resonances [33].

The reaction rate between $T = 0.1$ and 1 GK is characterized by the the EC and the contributions of the two narrow and isolated 3^- and 1^- resonances. The EC affects the reaction rate up to approximately 0.2 GK where the narrow resonances quickly become dominant. The overall rate is somewhat lower than that of NACRE [33] because of slightly lower values for the EC and the $\omega\gamma$ values of the two lowest-energy resonances.

Uncertainties in the reaction rate were calculated using the upper and lower bounds on the *S*-factor curve shown in Fig. 14 and the uncertainties associated with the resonance strengths $\omega\gamma$ and energies for the $E_\alpha = 1.1$ and 1.3 MeV resonances. Uncertainties from interference effects were also investigated for the higher energy resonances. Variation of these interference terms produced a change in the uncertainties of less than 3%.

VI. SUMMARY AND CONCLUSION

The $^{16}O(\alpha,\gamma)^{20}Ne$ reaction represents the end point for the α capture chain in stellar helium burning environments. The main uncertainty in the reaction rate has been the contribution of the $E2$ EC component which has been expected to dominate the reaction rate at stellar temperatures. Theoretical work predicted a whole range of values which are summarized in Table IV. This translated into a large uncertainty in the reaction rate predictions. To reduce the uncertainty on the low-energy *S* factor, a measurement of the excitation curve was performed by direct measurement using the RHINOCEROS gas target system at the Dynamitron laboratory at the University of

Stuttgart. The yield curve was normalized to the results of a measurement at the Nuclear Science Laboratory at the University of Notre Dame using a solid target of the same thickness to remeasure the yield curve over the large 0^+ resonance at $E_\alpha = 2.5$ MeV. The normalized (α,γ) yield curve for the radiative capture and the concurrently measured (α,α) elastic scattering cross section curve were then fit simultaneously using the R-matrix program AZURE. The fit yielded resonance widths Γ_{total} and strengths $\omega\gamma$ that were in good agreement with those quoted in the literature. The resulting fit and interference parameters were then combined with pre-existing higher-energy resonance information to extrapolate the cross section from $E_\alpha = 0.1$ to 10 MeV. A value of $S(300\text{ keV}) = 1.9(8+2)$ MeV b was extracted from the extrapolation representing a significant improvement in the uncertainty of the S factor. The extrapolation was then integrated numerically to calculate the reaction rate from $T = 0.1$ to 10 GK. The overall reaction rate is found to be slightly lower than that of the previous calculation [33]. The improved uncertainty on the S factor translated into a significant decrease in the uncertainty of the rate at low temperatures.

TABLE IV. Summary of all estimates of S(300 keV) for ^{16}O(α,γ)^{20}Ne. An average value of 2 MeV b was adopted by Ref. [33]. The values of S(300 keV) given by Refs. [7,8,34] and this work are semi-empirical calculations while those of Refs. [2,3,5,6] are theoretical predictions.

Ref.	Year	S(300 keV) MeV b
[34]	1975	0.4
[2]	1983	2.07
[3]	1986	2.54
[7]	1987	0.7
[5]	1988	1.7
[8]	1994	3.37[a]
[6]	2005	3.7(12)
This work		1.9(8 + 2)[b]

[a] Upper limit.

[b] Adopted first excited state EC branching ratio of 75(10)%.

ACKNOWLEDGMENTS

The authors would like to thank Heinrich Knee and Armin Mayer for the use of the data presented in their thesis works as well as Ralf Kunz for his considerable aid in the experimental work at the University of Stuttgart. This work was funded by the National Science Foundation through Grant No. Phys-0758100, and the Joint Institute for Nuclear Astrophysics Grant No. Phys-0822648. R.E.A. thanks the Natural Sciences and Engineering Research Council of Canada for support through the DRAGON grant at TRIUMF.

---

[1] F. K. Thielemann and W. D. Arnett, Astrophys. J. **295**, 604 (1985).
[2] K. Langanke, Phys. Lett. B **131**, 21 (1983).
[3] P. Descouvemont and D. Baye, Nucl. Phys. A **459**, 374 (1986).
[4] M. Dufour, P. Descouvemont, and D. Baye, Phys. Rev. C **50**, 795 (1994).
[5] D. Baye and P. Descouvemont, Phys. Rev. C **38**, 2463 (1988).
[6] P. Mohr, Phys. Rev. C **72**, 035803 (2005).
[7] K. H. Hahn, K. H. Chang, T. R. Donoghue, and B. W. Filippone, Phys. Rev. C **36**, 892 (1987).
[8] H. Knee, Ph.D. thesis, Universitat Stuttgart, 1994.
[9] A. Mayer, Ph.D. thesis, Universitat Stuttgart, 2001.
[10] J. D. MacArthur, H. C. Evans, J. R. Leslie, and H. B. Mak, Phys. Rev. C **22**, 356 (1980).
[11] J. W. Hammer, W. Biermayer, T. Griegel, H. Knee, and K. Petkau, RHINOCEROS, the Versatile Stuttgart Gas Target Facility (Part I), (unpublished).
[12] GEANT – Detector Description and Simulation Tool, CERN: Application Software Group, Computing and Networks Division, Geneva, Switzerland (1993).
[13] E. Strandberg *et al.*, Phys. Rev. C **77**, 055801 (2008).
[14] D. Phillips and J. P. S. Pringle, Nucl. Instrum. Methods **135**, 389 (1976).
[15] D. R. Tilley, C. M. Cheves, J. H. Kelley, S. Raman, and H. R. Weller, Nucl. Phys. A **636**, 249 (1998).
[16] P. M. Endt, Nucl. Phys. A **633**, 1 (1998).
[17] B. M. Paine and D. G. Sargood, Nucl. Phys. A **331**, 389 (1979).
[18] C. E. Rolfs and W. S. Rodney, *Cauldrons in the Cosmos*, 1st ed. (The University of Chicago Press, Chicago, 1988).
[19] J. F. Ziegler, J. P. Biersack, and M. D. Ziegler, SRIM: The Stopping and Range of Ions in Matter (2008) [www.srim.org].
[20] C. V. D. Leun, D. Sheppard, and P. Smulders, Phys. Lett. **18**, 134 (1965).
[21] J. W. Toevs, Nucl. Phys. A **172**, 589 (1971).
[22] R. T. Birge, Phys. Rev. **40**, 207 (1932).
[23] D. M. Van Patter and W. Whaling, Rev. Mod. Phys. **26**, 402 (1954).
[24] R. E. Azuma *et al.*, Phys. Rev. C **81**, 045805 (2010).
[25] A. M. Lane and R. G. Thomas, Rev. Mod. Phys. **30**, 257 (1958).
[26] E. Uberseder, R. deBoer, P. LeBlanc, E. Simpson, and R. Azuma, AZURE User Manual (2010) [azure.nd.edu].
[27] C. Angulo and P. Descouvemont, Nucl. Phys. A **690**, 755 (2001).
[28] A. M. Mukhamedzhanov, C. A. Gagliardi, and R. E. Tribble, Phys. Rev. C **63**, 024612 (2001).
[29] Z. Q. Mao, H. T. Fortune, and A. G. Lacaze, Phys. Rev. C **53**, 1197 (1996).
[30] W.-M. Yao *et al.*, J. Phys. G **33**, 1 (2006).
[31] Z. M. Szalata, K. Itoh, G. A. Peterson, J. Flanz, S. P. Fivozinsky, F. J. Kline, J. W. Lightbody, X. K. Maruyama, and S. Penner, Phys. Rev. C **17**, 435 (1978).
[32] J. Kopecky and M. Uhl, Phys. Rev. C **41**, 1941 (1990).
[33] C. Angulo *et al.*, Nucl. Phys. A **656**, 3 (1999).
[34] W. A. Fowler, G. R. Caughlan, and B. A. Zimmerman, Ann. Rev. Astron. Astrophys. **13**, 69 (1975).